PHYSICAL REVIEW B **100**, 054418 (2019)

Magnetic behavior and complete high-field magnetic phase diagram of the orthoferrite $ErFeO_3$

X. X. Zhang,[1] Z. C. Xia,[1,*] Y. J. Ke,[2] X. Q. Zhang,[3] Z. H. Cheng,[3,†] Z. W. Ouyang,[1] J. F. Wang,[1] S. Huang,[1] F. Yang,[1]
Y. J. Song,[1] G. L. Xiao,[1] H. Deng,[1] and D. Q. Jiang[1]
[1] *Wuhan National High Magnetic Field Center & School of Physics, Huazhong University of Science and Technology, 430074 Wuhan, China*
[2] *School of Science, Wuhan University of Technology, 430074 Wuhan, China*
[3] *State Key Laboratory of Magnetism and Beijing National Laboratory for Condensed Matter Physics, Institute of Physics, Chinese Academy of Sciences, Beijing 100190, China*

(Received 15 January 2019; revised manuscript received 4 June 2019; published 13 August 2019)

Magnetic transitions in a single crystal of the orthoferrite $ErFeO_3$ have been studied between 2 and 300 K using conventional superconducting quantum interference device measurements as well as pulsed high magnetic fields of up to 58 T. Spontaneous spin reorientations, as well as temperature and magnetic field induced spin reorientations, have been observed. At spin-reorientation transition temperatures, the Fe^{3+} sublattice exhibits a $\Gamma_4 \to \Gamma_2$ transition where the magnetic coupling between the net magnetic moment of Fe^{3+} $3d$ and Er^{3+} $4f$ is antiferromagnetic, and the temperature dependence of the magnetization suggests that the order of magnitude of the interaction is $J_{\text{Er-Er}} < J_{\text{Er-Fe}} < J_{\text{Fe-Fe}}$. However, the magnetic coupling varies widely with temperature and/or magnetic field, which indicates that the Er^{3+} sublattice moment cannot be simply explained by the partial polarization of the paramagnetic spins due to the combination of the molecular field from the net Fe^{3+} moment and external applied magnetic fields. It is found that in a sufficiently high magnetic field, the magnetic interactions between the Fe^{3+} sublattice and the Er^{3+} sublattice are destroyed. Based on the detailed magnetization measurements, the complete high-field magnetic phase diagram has been obtained, providing an important framework for future investigations into the complicated magnetic interactions and magnetoelectric couplings in rare earth orthoferrites.

DOI: 10.1103/PhysRevB.100.054418

I. INTRODUCTION

In recent years, orthoferrites $RFeO_3$ (where R is a rare earth element) with the *Pbnm* structure have gained renewed interest due to their unique properties such as laser-induced ultrafast spin reorientation [1,2], the giant anisotropic magnetocaloric effect [3–5], and multiferroicity [6–9]. A characteristic feature of $RFeO_3$ is the presence of two magnetic sublattices, the R^{3+} sublattice and the Fe^{3+} sublattice [10–13]. The Fe^{3+} sublattice usually orders into a canted antiferromagnetic (AFM) structure below the Néel temperature $T_N^{\text{Fe}} = 620-740$ K, which leads to a Néel vector G_x and a weak ferromagnetic (FM) vector F_z [14]. The net FM moment is usually very small (weak FM: wFM), but it plays an important role in the complex magnetic configuration, especially in the ordering of the R^{3+} sublattice and its spin reorientation transition (SRT). On the other hand, due to the high Néel temperature (>600 K) and the large magnetic moments of $Fe^{3+}(S = 5/2)$ ions, $RFeO_3$ compounds are considered as room-temperature multiferroic candidates with potentially high magnetoelectric (ME) coupling coefficients [15].

$ErFeO_3$ has a distorted perovskite crystal structure where its unit cell contains four magnetic Fe^{3+} ions forming AFM ordered sublattices, with a small canting angle due to the Dzyaloshinskii-Moriya interaction [16]. As shown in Fig. 1, at temperatures below T_N^{Fe}, the irreducible representation of the magnetic structure of the Fe^{3+} sublattice is $\Gamma_4(G_x, F_z)$, in which the F_z and G_x point along the c and a axis, respectively [14]. Within the SRT temperature interval $[T_2, T_1]$, $(T_2 < T_1 < T_N)$, the $ErFeO_3$ exhibits SRT from $\Gamma_4(G_x, F_z)$ to $\Gamma_2(G_z, F_x)$ [17]. The Er^{3+} sublattice is paramagnetic (PM) but partially polarized by the molecular field of the Fe^{3+} sublattice. Due to the interactions between the Er^{3+} and Fe^{3+} sublattices, as well as their different transition temperatures and dependences with respect to applied field and elastic stress, a wide array of complex SRTs can be observed in this system [2,18]. Usually, the net magnetic moment of the Er^{3+} ions is oriented antiparallel with respect to the net wFM moment of the Fe^{3+} sublattices and rotates by 90° together with a spin reorientation [19]. Bazaliy *et al.* suggested that the $\Gamma_4 \leftrightarrow \Gamma_2$ transition is second-order for most rare-earth orthoferrites [14]. Based on these symmetry configurations, it has been suggested that the magnetic moment can be rotated in the *ac* plane under an external magnetic field along the a or c axis. At temperatures below T_N^{Er}, the Er^{3+} moments align antiferromagnetically along the c axis with a C_z mode. Early studies suggest that there are two possible structures for Fe^{3+} moments: one for the Fe^{3+} moments in the *ac* plane and another one for the Fe^{3+} moments in the *bc* plane [20–23]. Nuclear magnetic resonance [24] and Mössbauer [25] measurements have provided evidence supporting the arrangement of the Fe^{3+} moments in the *bc* plane at temperatures below that of the Er^{3+} ordering temperature. Recently, based

---

[*] Author to whom correspondence should be addressed: xia9020@hust.edu.cn

[†] zhcheng@iphy.ac.cn

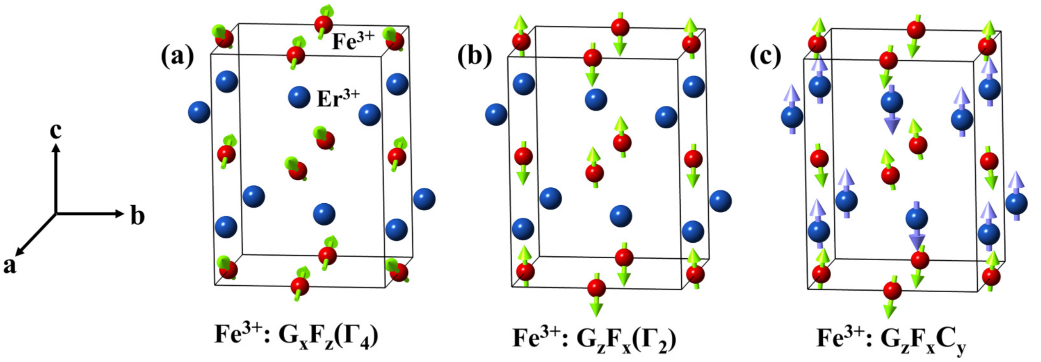

FIG. 1. Magnetic structure of ErFeO$_3$ in different temperature ranges (a) $T_1 < T < T_N^{Fe}$, (b) $T_N^{Er} < T < T_2$, (c) $T < T_N^{Er}$. Green arrows depict the Fe^{3+} moments, and blue arrows depict the Er^{3+} moments.

on a symmetry analysis from the refinement of diffraction results, at temperatures below T_N^{Er} another structure is suggested in which the Fe^{3+} magnetic moments maintain the same G_z and F_x modes, but an additional mode C_y is induced by the ordering of the Er^{3+} moments, i.e., they change from G_zF_x to $G_zF_xC_y$ [26]. One reason for this controversy is the complexity of the magnetic coupling between Fe^{3+} and R^{3+} sublattices, and the magnetic configurations of the compound have not been precisely described and are still debated. Since the multiferroic properties of this system strongly rely on the symmetry of the magnetic phases, it is necessary to accurately detail the magnetic structures and transitions in order to understand the possible ME mechanism in the materials. In particular, such a description of the magnetic configuration may no longer be sufficient in very high magnetic fields, which pull the sublattice magnetization towards the field direction eventually inducing the spin-flip/flop transition. The high magnetic field enables an additional rotation of the ferromagnetic vector on top of the spontaneous rotation and destroys (or partially destroys) the AFM interactions. Thus, an investigation of the magnetic anisotropy and magnetic configurations for RFeO$_3$ in a wide magnetic field range ($0 \sim 58$ T) may give us a deeper understanding of the magnetic contributions coming from the 4f electrons of rare earth R ions and the crystal structure. The findings of this investigation may be helpful for understanding the complicated magnetic configurations of the orthoferrites and their possible ME effect.

In this work, we performed precise measurements of the magnetization of a high quality ErFeO$_3$ single crystal in the temperature interval between 2 K and room temperature using a superconducting quantum interference device (SQUID) as well as a pulsed magnet of 58 T. The purpose is to reveal the magnetic configuration and interaction between the Fe^{3+} and Er^{3+} sublattices and investigate the different responses of these sublattices to various temperatures and magnetic fields.

II. EXPERIMENTAL

Polycrystalline rods of ErFeO$_3$ were synthesized by a conventional solid-state reaction method with a stoichiometric amount of Er$_2$O$_3$ (99.99%) and Fe$_2$O$_3$ (99.99%) as starting materials. A single crystal was grown by a Four Mirror Optical Floating Zone Furnace (Crystal Systems Corp.) with a growth rate of 3.5 mm/h in air. A single crystal sample $4 \sim 6$ mm in diameter and $3 \sim 5$ cm in length was obtained.

The crystal structures of the ErFeO$_3$ powder and single crystal samples were measured by an x-ray diffractometer (XRD, Philips X'pert pro). The low field magnetization behavior was measured in a static magnetic field (SQUID-VSM, Quantum Design), and the pulsed high magnetic field magnetization measurements, in the temperature range of 1.8–300 K, were performed at the Wuhan National High Magnetic Field Center using two concentric pick-up coils connected in series with opposite polarity. The pulsed high magnetic field in the shape of one half of a sine wave has a peak field of up to 58 T with a 30-ms pulse duration. Before each measurement, the sample was warmed above room temperature to remove any magnetic history.

III. RESULTS AND DISCUSSION

The XRD patterns of both the polycrystalline (crushed single crystal) and single crystal samples have been measured at room temperature. The diffraction pattern of a single crystal sample of ErFeO$_3$ is shown in Fig. 2, and its morphology is shown in the inset. As shown in Fig. 2, only (002)/(004)/(006) peaks are observed, showing the perfect c-axis orientation of the natural cleavage surface of the measured single crystal sample. The single crystal XRD pattern

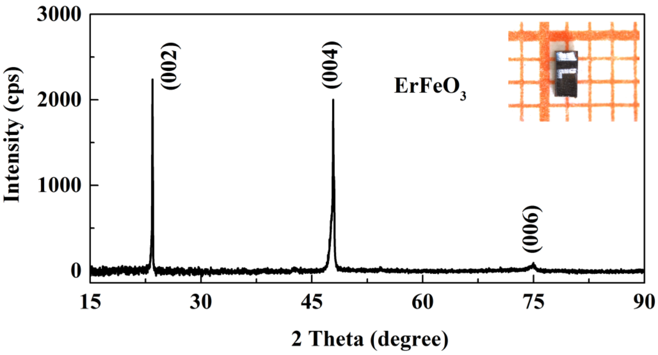

FIG. 2. Room temperature XRD patterns of the ErFeO$_3$ single crystal sample in which only (002)/(004)/(006) peaks are observed, showing their perfect c-axis orientation. The appearance of the single crystal sample is shown in the inset.

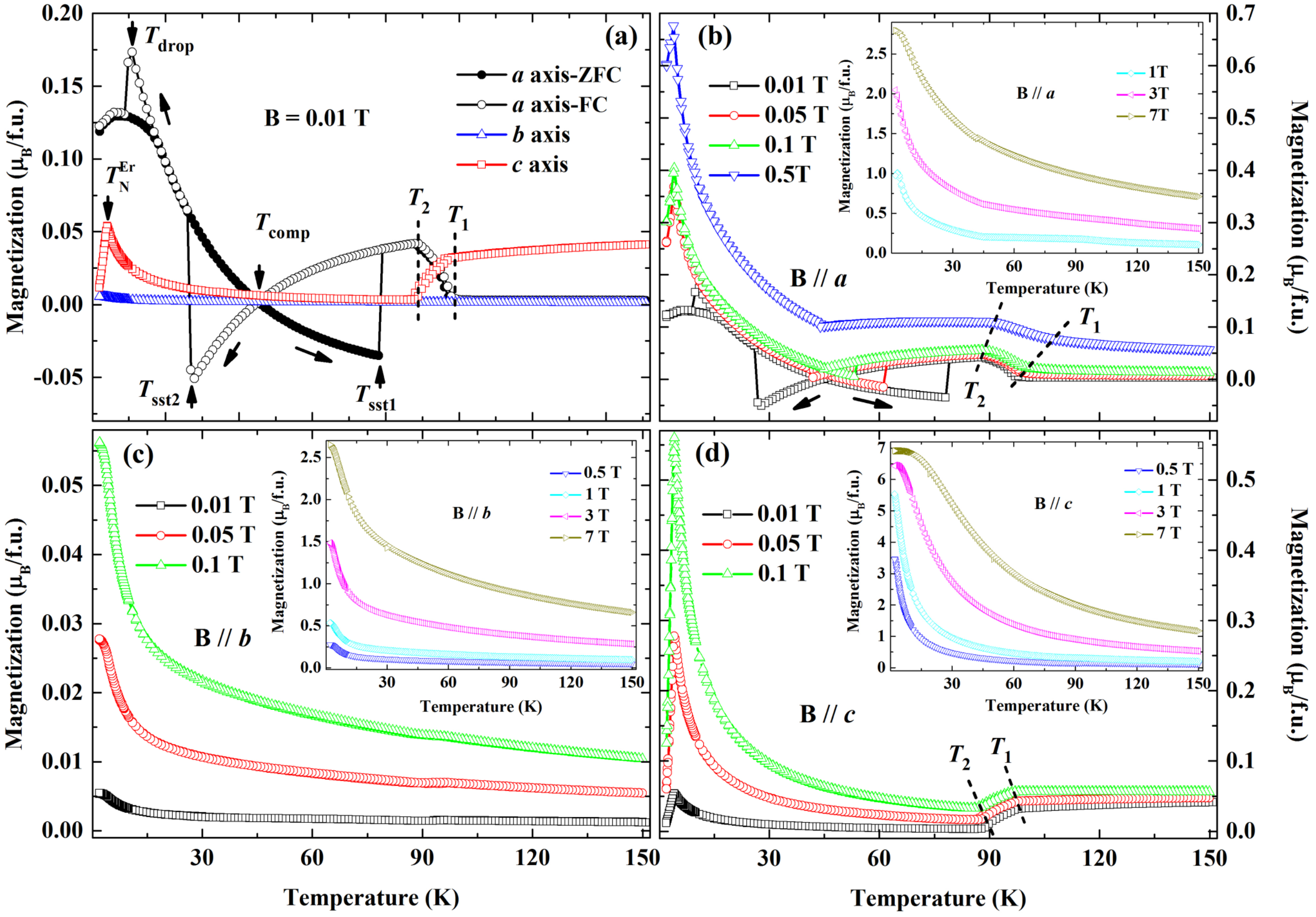

FIG. 3. (a) Temperature dependence of the magnetization of the ErFeO$_3$ single crystal along three principle axes measured in ZFC and FC processes under 0.01 T. (b)–(d) show the temperature dependence of magnetization measured under various magnetic fields for the ErFeO$_3$ single crystal along the *a*, *b*, and *c* axes, respectively.

demonstrates that the sample has a perfect crystal structure and lattice orientation.

The temperature dependence of the magnetization of ErFeO$_3$ measured at 0.01 T with both zero field cooling (ZFC) and field cooling (FC) modes is shown in Fig. 3(a). Different magnetization behaviors are observed when the magnetic field is applied along the *a* axis, *b* axis, and *c* axis, which confirm the strong magnetic anisotropy in the ErFeO$_3$ single crystal. When a magnetic field of 10 mT is applied along the *c* axis, the magnetization gradually decreases with decreasing temperature; as the temperature decreases from $T_1 = 98$ K to $T_2 = 89$ K the total magnetic moment changes from $\sim 0.035\ \mu_B$/f.u. at T_1 to $\sim 0.005\ \mu_B$/f.u. at T_2. Below T_2, a monotonic increase of magnetization with decreasing temperature is observed, which results from the PM behavior of the Er^{3+} sublattice. At $T_N^{Er} \sim 4.1$ K, a sharp drop in the magnetization is observed due to the AFM order of Er^{3+} sublattice. Below 4.1 K, the Er^{3+} sublattice has a magnetic configuration of C_z [26].

In the case where the same field is now applied parallel to the *a* axis, the magnetic moment is almost negligible above $T_1 (\sim 0.0038\ \mu_B$/f.u.). By decreasing the temperature from T_1 to T_2, the magnetic moment changes from $\sim 0.0038\ \mu_B$/f.u. at T_1 to $\sim 0.041\ \mu_B$/f.u. at T_2. These results, taken in combination with the magnetic moment analysis of the field along the *c* axis, reveal that as the temperature decreases from T_1 to T_2 the magnetic moment rotates from *c* axis to *a* axis, i.e., the system experiences a SRT between T_1 and T_2 [17]. In the FC mode, with decreasing temperature the magnetic moment monotonically decreases, and it becomes zero at the so-called compensation temperature $T_{comp} (\sim 44.8$ K) where the net magnetic moment of the Fe^{3+} sublattice is canceled by the antiparallel magnetic moment of the Er^{3+} sublattice. By further decreasing the temperature to $T < T_{comp}$, the moment of the Er^{3+} sublattice dominates that of the Fe^{3+} sublattice, and the total magnetization becomes negative. At the temperature $T_{sst2} \sim 26$ K, a magnetization jump is observed in which the magnetic moment changes from $-0.05\ \mu_B$/f.u. to $+0.05\ \mu_B$/f.u., indicating a simultaneous spin-flip of the magnetic moments of both the Er^{3+}- and Fe^{3+} sublattices, i.e. a spin switching transition (SST) occurs at T_{sst2} [10]. Although the direction of the net magnetic moment direction reverses at the T_{sst2}, the absolute value of the net magnetic moment is not changed. This means that the magnetic coupling between the Er^{3+} sublattice and Fe^{3+} sublattice along the *a* axis is always AFM. The strong antiparallel coupling between the wFM, canted AFM Fe^{3+} sublattice and Er^{3+} sublattice indicates that the magnetic moment of the Er^{3+} sublattice cannot be

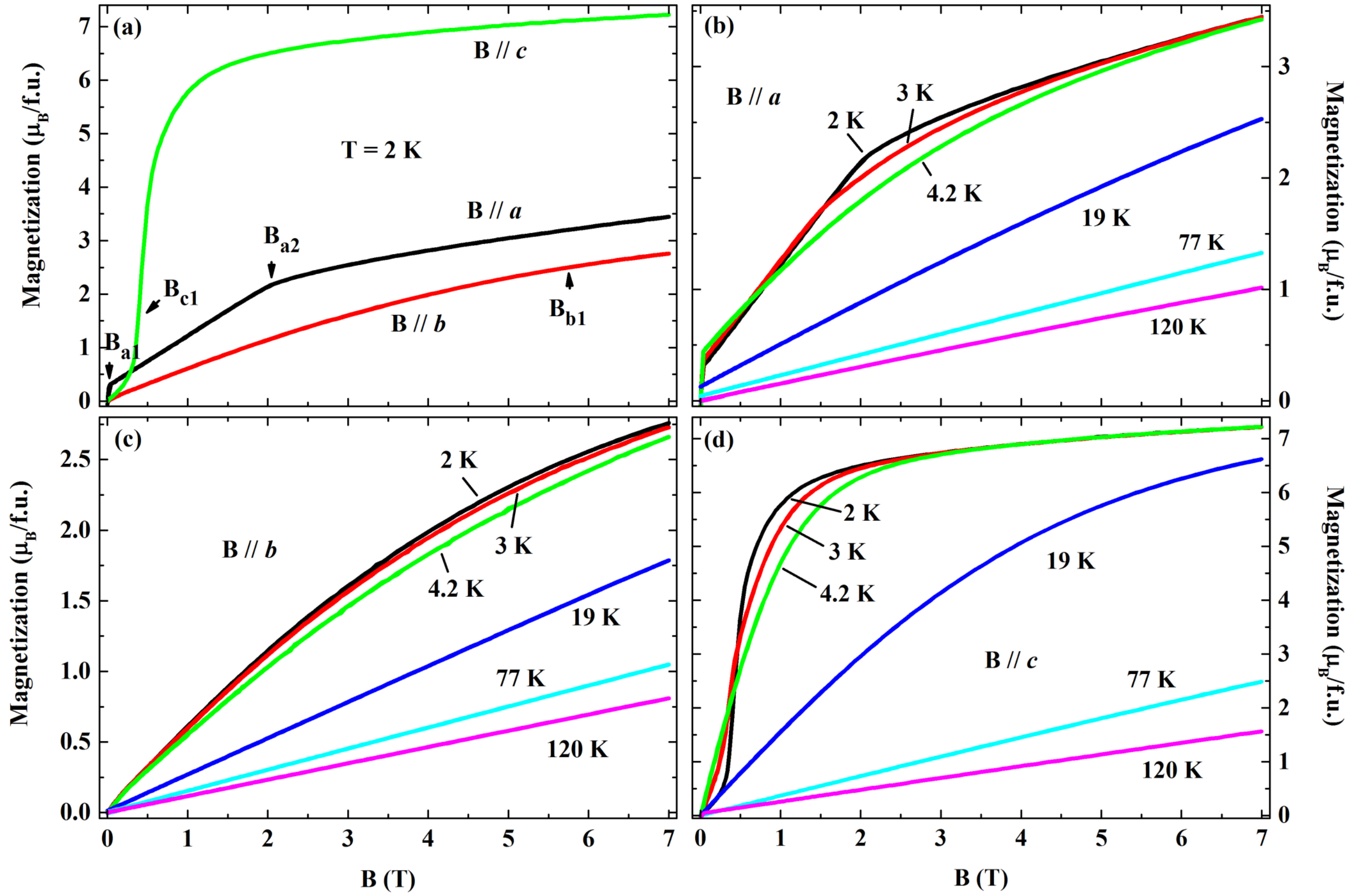

FIG. 4. (a) The magnetization of $ErFeO_3$ as a function of magnetic field along the *a*, *b*, and *c* axes at 2 K. (b)–(d) the evolution of $M(B)$ curves with changing temperature for $ErFeO_3$ in magnetic fields along the *a*, *b*, and *c* axes, respectively.

explained simply by the PM state being partially polarized by the molecular field of the Fe^{3+} sublattice, implying that an additional Fe^{3+} $3d$$-$$Er^{3+}$ $4f$ magnetic coupling may exist [27]. On further cooling, an abrupt drop is observed at $T_{\text{drop}} \sim 10$ K in the FC mode, which is similar to that reported in Ref. [28]. In the ZFC process, the anomaly at T_{drop} disappears and the critical temperature of the SST moves to a higher temperature $T_{\text{sst1}} = 78$ K. There is a significant hysteresis between the FC mode and ZFC mode, indicating that the SST is a first-order transition. For the final situation in which the field is applied parallel to the *b* axis, there is no significant change in the magnetization intensity throughout the entire temperature interval, although a slight increase at low temperature (below 10 K) may result from a PM impurity and/or the contribution from the smaller magnetic moment component of the *a* axis (*c* axis). This indicates that the magnetic moments are mainly localized in the *ac* plane; in particular, these experimental results confirm that the SRT and SST occur almost exclusively within the *ac* plane [14].

In $ErFeO_3$, the Fe^{3+} and Er^{3+} sublattices have quite different properties, which is shown by their different dependences on temperature and magnetic field. Usually, the application of a magnetic field has a dual effect: (i) it polarizes the Er^{3+} sublattice and (ii) it induces the SRT of the $\Gamma_2 \rightarrow \Gamma_4$ in the Fe^{3+} sublattice. In order to investigate the effects of the applied magnetic field on magnetization behavior, the temperature dependence of magnetization was measured as a function of applied magnetic field. As shown in Figs. 3(b)–3(d), the magnetization of the $ErFeO_3$ single crystal along three crystallographic axes is indicative of anisotropic behavior. For the magnetic field along the *a* axis as shown in Fig. 3(b), both T_{ss1} and T_{ss2} shift toward T_{comp} with increasing magnetic field, and when above 0.1 T the SST is totally suppressed and the negative net magnetization disappears. Meanwhile, the SRT tends to take place at higher temperatures with increasing magnetic field strength. In contrast, as shown in Fig. 3(d), when the magnetic field is applied parallel with the *c* axis the spin reorientation temperature (T_1 and T_2) moves to lower temperatures with increasing field. This means that the application of a magnetic field can modify the anisotropy interaction between Er^{3+} and Fe^{3+} electrons. Above 0.5 T, as shown in the insets of Fig. 3, the SRT is totally suppressed by the applied magnetic field. For a magnetic field applied parallel to the *b* axis, no significant abnormalities are observed even when the magnetic field increased to 7 T.

The magnetic field dependence of the magnetizations measured at static magnetic field with selected temperatures are shown in Fig. 4. At 2 K (below T_N^{Er}), the magnetization curves measured with field parallel to the three principal axes are shown in Fig. 4(a), where the dramatically anisotropic behavior is observed. For an applied field parallel to the *a* axis, a spontaneous magnetic moment ($\sim$0.3 μ_B/f.u.) is observed that aligns along the direction of the magnetic field around $B_{a1} \sim 0.03$ T. This result shows that the easy magnetization direction is the a axis ($\mathrm{Fe}^{3+}: G_zF_x$, where the x means the a axis). It is well known that the magnetic field causes an additional rotation of the magnetic moment on top of the spontaneous rotation. With increasing magnetic field, the magnetization increases linearly showing an AFM behavior. Considering the magnitude of the interactions: $J_{\text{Er-Er}} < J_{\text{Er-Fe}} < J_{\text{Fe-Fe}}$ [29], the observed AFM behavior is mainly related to the spin-flop of the AFM Er^{3+} sublattice due to the weak magnetic interaction of $J_{\text{Er-Er}}$. As the magnetic field increases to $B_{\mathrm{a2}} \sim 2.1$ T, it is observed that the slope of the $M_{\mathrm{a}}(B)$ curve changes significantly: above B_{a2}, the slope becomes smaller, indicating a stronger AFM coupling. As shown in Fig. 4(a), the magnetic moment at B_{a2} is $\sim 2.2\ \mu_{\mathrm{B}}/\mathrm{f.u.}$, which is much smaller than the effective magnetic moment of the Er^{3+} sublattice ($\sim 9.5\ \mu_{\mathrm{B}}/\mathrm{Er}^{3+}$). This result indicates that the AFM coupling of the Er^{3+} sublattice is not destroyed completely, and the change in the slope of the $M_{\mathrm{a}}(B)$ curve at B_{a2} is likely a reflection of the magnetic transition in the ac plane, where spins are triggered by the mutual induction of the magnetic moments of Fe^{3+}-$3d$ and Er^{3+}-$4f$ orderings in the strong magnetic fields [30]. The ordered Er^{3+} sublattice has a strong effect on the magnetic behavior of the Fe^{3+} sublattice due to the effective field of the ordered Er^{3+} sublattice. By further increasing the magnetic field, a linear magnetization behavior is observed, showing a dominant AFM ordering, which results from the both the internal AFM orderings of the Er^{3+} sublattice and Fe^{3+} sublattice, as well as the AFM interaction between the Er^{3+} and Fe^{3+} sublattices. For an applied field parallel to the c axis, a state with near zero magnetic moment is observed at lower magnetic field, suggesting that the net magnetic moments of both the Er^{3+} and Fe^{3+} sublattice are not along the c axis, consistent with the magnetic configuration of the mixture of $\mathrm{Fe}^{3+}: G_zF_x$ and $\mathrm{Er}^{3+}: C_z$. With increasing magnetic field, a metamagnetic transition is observed at $B_{\mathrm{c1}} \sim 0.4$ T. According to the magnetic configuration of the mixture of $\mathrm{Fe}^{3+}: G_zF_x$ and $\mathrm{Er}^{3+}: C_z$, the metamagnetic transition results from the spin reorientation of $\mathrm{Er}^{3+}: C_z \rightarrow F_z$ due to the weaker AFM interaction of $J_{\text{Er-Er}}$ [31]. With increasing magnetic field, the AFM coupling of the Er^{3+} sublattice changes to canted AFM and then to FM ordering, where the higher magnetic moment ($\sim 7.5\ \mu_{\mathrm{B}}/\mathrm{f.u.}$) suggests that the FM coupling is dominant in the Er^{3+} sublattice when the magnetic field is above B_{c1}. These experimental results are in good agreement with the estimated value of the magnetic moment of $\mathrm{ErFeO_3}$ [23], in which the spontaneous weak FM order results mainly from the canted AFM of Fe^{3+} sublattice. At 1.3 K and 1.25 T, the magnetization attains $5.7\ \mu_{\mathrm{B}}/\mathrm{f.u.}$ when magnetized along the c axis, whereas along the a axis it is only $0.4\ \mu_{\mathrm{B}}/\mathrm{f.u.}$ and decreasing with lowering temperature. A neutron diffraction study has confirmed that, at liquid helium temperatures, the Er^{3+} ion moments in $\mathrm{ErFeO_3}$ form a nearly ideal AFM configuration [21]. Thus, the spontaneous weak FM observed at low temperature originates mainly from the Fe^{3+} sublattice. For the field parallel to the b axis, only a slight change of the magnetization slope is observed at $B_{\mathrm{b1}} \sim 5.8$ T, and the value of the magnetization is the smallest among the three principal axes indicating that the easy magnetization direction is not along the b axis and that the magnetic moments are mainly confined in the ac plane. This magnetic transition can be clearly distinguished in pulsed high magnetic fields due to the high $\mathrm{d}B/\mathrm{d}t$ enhancing the sensitivity of the magnetization measurement. Figure 5(b) shows clearly the transition at the magnetic field B_{b1}. The antisymmetric exchange energy responsible for the canting of the moments of Fe^{3+} sublattice gives rise to an effective field of the order of 10^5 Oe, which acts to confine the net moment to the ac plane [32]. Thus, the transition observed at $B_{\mathrm{b1}} \sim 5.8$ T (the magnetic field is smaller than 10^5 Oe) should not result from the Fe^{3+} sublattice, and we assume it is directly related to the Er^{3+} sublattice. Since the magnetic field direction (along the b axis) is perpendicular to the magnetic vectors of Er^{3+} spins (within the ac plane), the applied magnetic field pulls the Er^{3+} spins away from the ac plane and rotates the magnetic vectors of Er^{3+} spins towards the magnetic field direction (b axis) as much as possible, eventually leading to a spiral magnetic configuration. Similar magnetic-field-induced AFM to spiral ordering transitions were observed in triangular antiferromagnets, such as $\mathrm{Ba_3CoSb_2O_9}$ and $\mathrm{Cs_2CuBr_4}$ [33,34]. The evolution of the $M_a(B)$, $M_b(B)$, and $M_c(B)$ curves with temperature are shown in Figs. 4(b)–4(d), respectively. With increasing temperature (above $T_{\mathrm{N}}^{\mathrm{Er}}$), the Er^{3+} moments become PM states, thus all the transitions related to the AFM ordering of the Er^{3+} sublattice disappear naturally. In other words, the magnetic transitions at B_{a2}, B_{b1}, and B_{c1} are dominated by Er^{3+} moments in the lower temperature region. For the applied field parallel to the a axis as shown in Fig. 4(b), a weak FM ordering is still observed near zero field at 19 K that results from the net weak FM of the G_zF_x configuration of the Fe^{3+} sublattice and the polarized PM of the Er^{3+} sublattice. The linear magnetization behavior shows the coexistence of both the PM of the Er^{3+} sublattice and AFM of the Fe^{3+} sublattice. By further increasing the temperature to 77 and 120 K, linear magnetization curves are observed with the magnetic field applied respectively along all three principal axes, indicating the strong AFM and/or PM behavior. The magnetization values measured with the field parallel to both the c axis and a axis are higher than those measured when the field is parallel to the b axis, which shows that the moments of the Er^{3+} sublattice and Fe^{3+} sublattice are mainly confined in the ac plane.

Usually, an applied magnetic field causes additional rotation of the magnetic moments beyond that obtained from spontaneous rotation. In particular, high magnetic fields tend to pull the magnetic moments of the Fe^{3+} sublattice and the Er^{3+} sublattice towards the direction of the magnetic field as far as possible, eventually resulting in spin flop/flip transitions for $\mathrm{ErFeO_3}$. Therefore, the low magnetic field structures described previously may no longer be suitable when considering results measured at very high fields. In order to study the effect of high magnetic field on the magnetic configuration of the $\mathrm{ErFeO_3}$ single crystal, the magnetization behavior of the $\mathrm{ErFeO_3}$ single crystal was measured across a wide range of temperatures with a pulsed high magnetic field of 58 T. Figures 5(a)–5(c) show the high-field magnetization curves measured at $T = 2$ K with the magnetic field along the a, b, and c axis, respectively. The low field phase transition becomes easier to be distinguished, and additional high-field-induced phase transitions are observed as well. All of the critical fields for these phase transitions are determined by the differential of the magnetization over the magnetic field

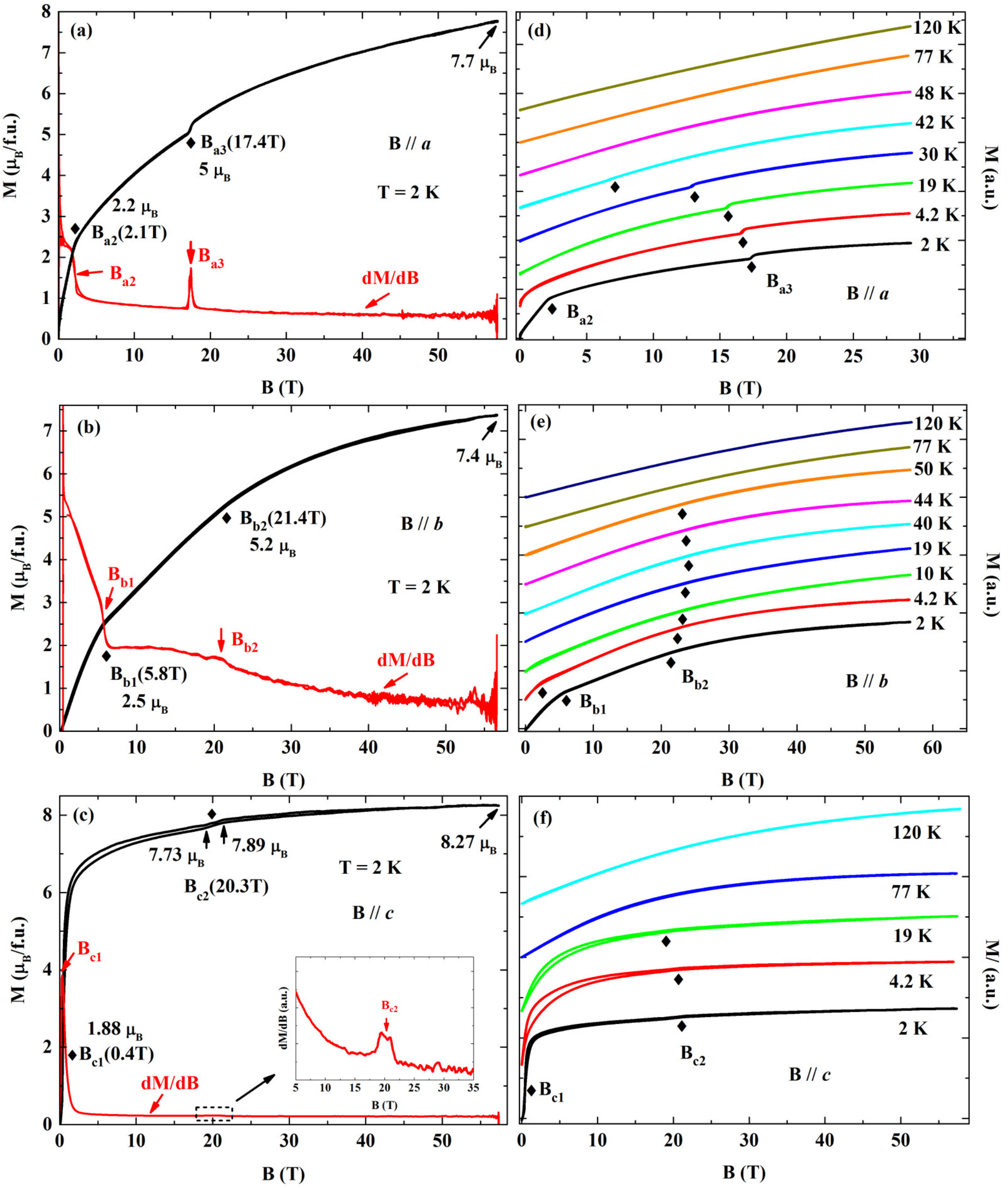

FIG. 5. (a)–(c) High-field magnetization of the $\mathrm{ErFeO_3}$ single crystal at 2 K with applied field along the *a*, *b*, and *c* axes, respectively. The magnetization data were calibrated by the SQUID data. The derivative $\mathrm{d}M/\mathrm{d}B$ of the pulsed high magnetic field magnetization curves are shown at the bottom and the arrows indicate the magnetic transition fields. (d)–(f) the evolution of the magnetic transitions with temperature for $B//a$, $B//b$, and $B//c$, respectively. The solid rhombuses show the phase transition fields and the curves are offset for clarity.

($\mathrm{d}M/\mathrm{d}B$). With the magnetic field parallel to the *a* axis, as shown in Fig. 5(a), by increasing the magnetic field to $B_{a3} \sim 17.4$ T a transition is observed corresponding to a magnetic moment of $\sim 5\ \mu_{\mathrm{B}}/\mathrm{f.u.}$, which is less than the theoretical saturation magnetic moment of the $\mathrm{Er^{3+}}$ sublattice. The unsaturated magnetic moment indicates that the spin-flop plays a leading role in the transition process and induces canted AFM states (the vector of the net magnetic moment of the canted AFM is along the *a* axis) rather than FM states in higher magnetic fields. When the magnetic field is larger than the critical field B_{a3}, a jump-like phase transition occurs, which may be due to the change of the net moment of the canted $\mathrm{Fe^{3+}}$ sublattice transitioning from an AFM interaction with the $\mathrm{Er^{3+}}$ sublattice to a FM interaction under the influence of a high magnetic field. Above B_{a3}, the field-induced polarization of the $\mathrm{Er^{3+}}$ sublattice and spin-flop of the AFM $\mathrm{Fe^{3+}}$ sublattice lead to a linear magnetization behavior and a higher magnetic moment. As shown in Fig. 5(d), the two phase transitions show different temperature dependences, where the phase transition of B_{a2} becomes more difficult to discern, and the phase transition field of B_{a3} shifts to the lower fields. As the temperature rises to $T = 48$ K, above T_{comp}, this magnetic transition completely disappears indicating the wFM of the Fe sublattice aligns along the direction of the applied field.

As shown in Fig. 5(c), an additional transition occurs at $B_{c2} \sim 20.3$ T when the applied field is parallel to the *c* axis. With this phase transition, the magnetic moment changes from

7.73 to 7.89 μ_B/f.u., which may be due to the breakdown of the AFM interaction between the canted Fe^{3+} sublattices and the partially polarized Er^{3+} sublattices. Therefore, the external magnetic field causes the net magnetic moment vector of the Fe^{3+} sublattice and partially polarized Er^{3+} sublattice to align with the direction of the external magnetic field, i.e., the magnetic configurations change to Fe : G_xF_z and Er : F_z. With increasing magnetic field, the C_z phase of the Er^{3+} sublattice is almost polarized, leading to a higher magnetic moment of ∼8 μ_B/f.u. As shown in Fig. 5(f), with increasing temperature the additional phase transition becomes smooth, and the critical field B_{c2} moves towards lower magnetic field. At lower temperatures, smaller hysteresis is observed possibly due to the large magnetocaloric effect in $ErFeO_3$ [3]. At 77 and 120 K as shown in Fig. 5(f), a similar behavior of the magnetization is observed in which the parabolic magnetization curves show the dominant AFM ordering (Fe^{3+} sublattice) and a coexistent weak FM ordering (polarized PM state of Er^{3+} sublattice).

Figure 5(b) shows the magnetization curve obtained with the magnetic field applied parallel to the *b* axis, and two transitions are observed at $B_{b1} \sim 5.8$ T and $B_{b2} \sim 21.4$ T. As mentioned above, at zero field the magnetic vector of the $Er^{3+} : C_z$ is along the *c* axis, which is a nearly ideal AFM configuration [21], while the AFM vector is perpendicular to the external field direction (*b* axis). By increasing the magnetic field to B_{b1}, the $Er^{3+} : C_z$ state is gradually destroyed and changes to the spiral magnetic configuration. Above B_{b1}, the magnetization increases due to the net magnetic moment of the spiral Er^{3+} sublattice increasing linearly from the spin-flop. When the applied field is increased to B_{b2}, this corresponds to a confined effective field on the order of 10^5 Oe [32] and the external magnetic field pulls the magnetic moments of the Fe^{3+} sublattice away from the *ac* plane leading to a spiral magnetic configuration with the magnetic vector parallel to the magnetic field direction (*b* axis). This scenario is similar to that the high-field-induced spiral ordering observed in the frustrated magnet $CuFeO_2$ [35] and the two-dimensional tetragonal compound $TlCo_2Se_2$ [36], in which the external magnetic field drives the magnetic moments of Fe^{3+} ions ($CuFeO_2$) and Co^{2+} ions ($TlCo_2Se_2$) away from the easy plane. With stronger magnetic fields, the angle between the magnetic vector and easy plane increases and the spiral magnetic configuration is formed. At temperatures above 4.2 K, as shown in Fig. 5(e), only one transition is observed at B_{b2}. The lower field transitions resulting from the AFM order of Er^{3+} sublattice naturally disappear due to the high temperature PM behavior of the Er^{3+} sublattice.

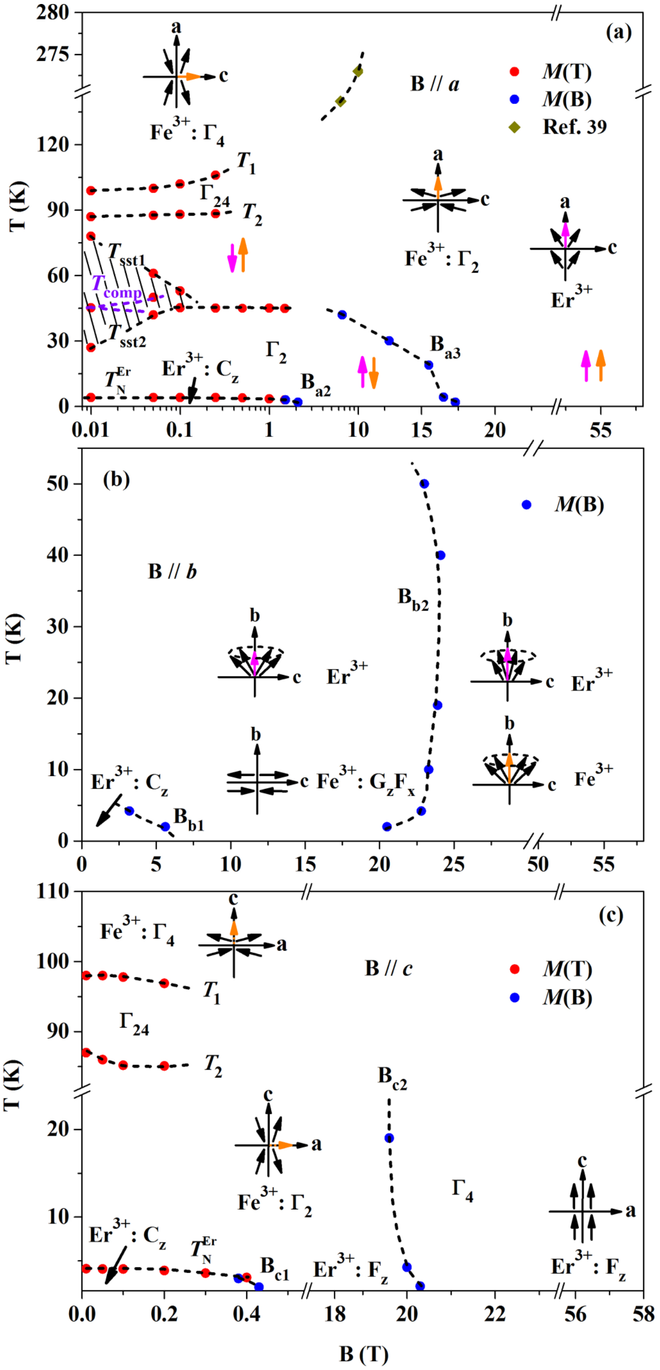

FIG. 6. High-field phase diagrams of the $ErFeO_3$ single crystal for (a) $B//a$ axis, (b) $B//b$ *axis*, and (c) $B//c$ *axis*. The black and orange arrows denote the Fe^{3+} spins and the net magnetic moment of the Fe^{3+} sublattice, the black and magenta arrows denote the Er^{3+} spins and the net magnetic moment of the Er^{3+} sublattice.

Usually, in zero or weak magnetic fields, spins rotate within the easy axis (plane) and thus the axis of spin rotation is parallel to the hard axis of a magnet. In high magnetic fields, spins prefer to rotate around the applied magnetic field direction where the high magnetic field drives the spin-rotation axis to flop/flip and induces a complex transition. In $ErFeO_3$, under low magnetic fields, the net magnetic moments of the canted AFM Fe^{3+} sublattice are confined in the *ac* plane. With the increase of magnetic field, the magnetic moment of the canted Fe^{3+} sublattice is expected to be pulled away from the *ac* plane when an adequate magnetic field is applied along the *b* axis, eventually leading to spiral states with the vector along the *b* axis. Similar magnetic field-induced spin spiral configurations have been observed in many frustrated magnets [35,37,38]. In addition, Mössbauer spectra showed the SRT of type $\Gamma_4(G_xF_z)$ to $\Gamma_2(G_zF_x)$ of Fe^{3+} sublattice could be driven by the magnetic field along the *a* axis above T_1 [39]. Our results indicate that the wFM of the Fe^{3+} sublattice reorients from the *a axis* back to the *c axis* [from $\Gamma_2(G_zF_x)$ to $\Gamma_4(G_xF_z)$] when the external field is parallel to the c axis at the temperature below T_2. This interpretation can be understood based on the effective field model [29], where the anisotropic effective field acts on the Fe^{3+} spins and favors the $\Gamma_2(G_zF_x)$ configuration below T_2. When the field is applied along the c axis, the magnetic field weakens the exchange interaction energy between Fe^{3+} and Er^{3+} spins in $\Gamma_2(G_zF_x)$, and strengthens the interaction energy in $\Gamma_4(G_xF_z)$. Therefore, the interaction energy with the effective field of a $\Gamma_4(G_xF_z)$ type exceeds that of the Fe^{3+} anisotropy energy, aided by the interaction energy with the effective fields of $\Gamma_2(G_zF_x)$ type under sufficient applied field, in turn leading to the field-driven $\Gamma_2(G_zF_x) \rightarrow \Gamma_4(G_xF_z)$ phase transition [40]. With increasing temperature, the effective anisotropy field decreases due to the PM behavior of the Er^{3+}-magnetic moments. Consequently, the critical field B_{c2} moves to lower field with increasing temperature as shown in Fig. 5(f). Above 77 K, no significant spin reorientation transitions are found, which may result from the higher thermal energy becoming competitive with the interaction energy.

Based on the magnetization measurements with static and pulsed high magnetic fields, the complete magnetic phase diagrams of the $ErFeO_3$ single crystal along three principal axes were obtained. As shown in Fig. 6, in the low magnetic field region when the temperature is lower than T_N^{Fe}(~636 K) [41] the weak net magnetic moment of the canted Fe^{3+} sublattice rotates from the c axis to a axis, resulting in the SRT of Fe^{3+} sublattice from $\Gamma_4(G_x, F_z)$ to $\Gamma_2(G_z,\ F_x)$ in the temperature region of T_2(89 K) to T_1(98 K). Namely, the magnetization rotation is mainly confined in the ac plane, which is consistent with the reference results [14]. As the temperature decreases to T_{sst2}, the SST transition takes place in which both the moments of the Er^{3+} and Fe^{3+} sublattices switch simultaneously. Below this temperature, the polarized Er^{3+} sublattices couples antiferromagnetically with the wFM of the Fe^{3+} sublattice. Due to the influences of temperature and external magnetic field, the induced FM of Er^{3+} sublattice is in competition with the wFM formed by the canted AFM state of Fe^{3+} sublattice causing a complex magnetic interaction in $ErFeO_3$. Only for sufficiently low temperatures and small external magnetic fields is the Er^{3+} sublattice able to adopt an ideal AFM configuration ($Er^{3+}: C_z$ at $T < T_N^{Er}$) [21]. At lower temperatures and stronger magnetic fields, the net weak FM of the canted Fe^{3+} sublattice is induced and aligns along the magnetic field direction as much as possible. By further increasing the applied field strength the AFM coupling of the Er^{3+} sublattices is gradually destroyed, accompanied by the destruction of the AFM interaction between the Er^{3+} and Fe^{3+} sublattices as well. At higher fields (above B_{a3}, B_{b2} and B_{c2}), the Er^{3+} sublattices are almost completely polarized and the AFM coupling between the Er^{3+} and Fe^{3+} sublattices is gradually weakened. Consequently, the Fe^{3+} sublattice shows the canted AFM order when the magnetic field is applied along the a axis and c axis, as well as spiral order when the magnetic field is applied along the b axis.

IV. CONCLUSION

Using static and pulsed high magnetic fields, we investigated the magnetization behaviors of an $ErFeO_3$ single crystal in the magnetic field range of 0–58 T and in the temperature range of 2–300 K. The complete high-field magnetic phase diagram of the $ErFeO_3$ single crystal along three principle axes has been obtained, extending to higher magnetic fields than previously reported, to the best of our knowledge. At lower temperatures (below 4.1 K) and lower magnetic fields (below 7 T), the magnetic behaviors of $ErFeO_3$ are dominated by Er^{3+} spins. Above T_N^{Er}, the Er^{3+} sublattice is in the PM state but polarized antiferromagnetically with the wFM of Fe^{3+} sublattice. In addition to the temperature induced SRT between T_1(98 K) and T_2(89 K), the SRT of type $\Gamma_2(G_zF_x) \leftrightarrow \Gamma_4(G_xF_z)$ also can be driven by the external field applied along the c axis or a axis. In a sufficiently high applied field ($B > B_{a3} \sim 17.4$ T, $B_{b2} \sim 21.4$ T, $B_{c2} \sim 20.3$ T for field along a, b, c axis, respectively), the strong magnetic coupling between the Fe^{3+} sublattice and Er^{3+} sublattice is destroyed, resulting in similar magnetic configurations among the three principal axes. Some results regarding the magnetic states are still speculative although they are based on our careful analysis of the magnetization measurements. Further investigations by other direct experimental techniques are necessary to clarify the anisotropy and magnetic configurations.

ACKNOWLEDGMENTS

This work was supported in part by the National Key R&D Program of China (Grant No. 2016YFA0401003), the National Natural Science Foundation of China (Grants No. 11674115, No. 51861135104, No. 11104091, No. 11704294, and No.11474110) and the Fundamental Research Funds for the Central Universities (Grant No. 2018KFYXKJC010). We thank E. Vetter for his linguistic assistance in the revision of this manuscript.

---

[1] A. V. Kimel, A. Kirilyuk, A. Tsvetkov, R. V. Pisarev, and Th. Rasing, Nature (London) **429**, 850 (2004).

[2] J. A. de Jong, A. V. Kimel, R. V. Pisarev, A. Kirilyuk, and Th. Rasing, Phys. Rev. B **84**, 104421 (2011).

[3] R. X. Huang, S. X. Cao, W. Ren, S. Zhan, B. J. Kang, and J. C. Zhang, Appl. Phys. Lett. **103**, 162412 (2013).

[4] Y. J. Ke, X. Q. Zhang, Y. Ma, and Z. H. Cheng, Sci. Rep. **6**, 19775 (2016).

[5] Y. J. Ke, X. Q. Zhang, J. F. Wang, and Z. H. Cheng, J. Alloys Compd. **739**, 897 (2018).

[6] Y. Tokunaga, N. Furukawa, H. Sakai, Y. Taguchi, T. Arima, and Y. Tokura, Nat. Mater. **8**, 558 (2009).

[7] Y. Tokunaga, S. Iguchi, T. Arima, and Y. Tokura, Phys. Rev. Lett. **101**, 097205 (2008).

[8] Y. Tokunaga, Y. Taguchi, T. Arima, and Y. Tokura, Phys. Rev. Lett. **112**, 037203 (2014).

[9] Z. Y. Zhao, X. Zhao, H. D. Zhou, F. B. Zhang, Q. J. Li, C. Fan, X. F. Sun, and X. G. Li, Phys. Rev. B **89**, 224405 (2014).

[10] S. J. Yuan, W. Ren, F. Hong, Y. B. Wang, J. C. Zhang, L. Bellaiche, S. X. Cao, and G. Cao, Phys. Rev. B **87**, 184405 (2013).

[11] L. T. Tsymbal, Ya. B. Bazaliy, V. N. Derkachenko, V. I. Kamenev, G. N. Kakazei, F. J. Palomares, and P. E. Wigen, J. Appl. Phys. **101**, 123919 (2007).

[12] S. E. Hahn, A. A. Podlesnyak, G. Ehlers, G. E. Granroth, R. S. Fishman, A. I. Kolesnikov, E. Pomjakushina, and K. Conder, Phys. Rev. B **89**, 014420 (2014).

[13] S. E. Nikitin, L. S. Wu, A. S. Sefat, K. A. Shaykhutdinov, Z. Lu, S. Meng, E. V. Pomjakushina, K. Conder, G. Ehlers, M. D. Lumsden, A. I. Kolesnikov, S. Barilo, S. A. Guretskii, D. S. Inosov, and A. Podlesnyak, Phys. Rev. B **98**, 064424 (2018).

[14] Ya. B. Bazaliy, L. T. Tsymbal, G. N. Kakazei, A. I. Izotov, and P. E. Wigen, Phys. Rev. B **69**, 104429 (2004).

[15] J.-H. Lee, Y. K. Jeong, J. H. Park, M.-A. Oak, H. M. Jang, J. Y. Son, and J. F. Scott, Phys. Rev. Lett. **107**, 117201 (2011).

[16] J. Jiang, G. Song, D. Wang, Z. Jin, Z. Tian, X. Lin, J. Han, G. Ma, S. Cao, and Z. Cheng, J. Phys.: Condens. Matter **28**, 116002 (2016).

[17] L. T. Tsymbal, V. I. Kamenev, Ya. B. Bazaliy, D. A. Khara, and P. E. Wigen, Phys. Rev. B **72**, 052413 (2005).

[18] H. Shen, Z. X. Cheng, F. Hong, J. Y. Xu, S. J. Yuan, S. X. Cao, and X. L. Wang, Appl. Phys. Lett. **103**, 192404 (2013).

[19] R. V. Mikhaylovskiy, T. J. Huisman, R. V. Pisarev, Th. Rasing, and A. V. Kimel, Phys. Rev. Lett. **118**, 017205 (2017).

[20] R. L. White, J. Appl. Phys. **40**, 1061 (1969).

[21] W. C. Koehler, E. O. Wollan, and M. K. Wilkinson, Phys. Rev. **118**, 58 (1960).

[22] G. Gorodetsky, R. M. Hornreich, I. Yaeger, H. Pinto, G. Shachar, and H. Shaked, Phys. Rev. B **8**, 3398 (1973).

[23] R. M. Bozorth, V. Kramer, and J. P. Remeika, Phys. Rev. Lett. **1**, 3 (1958).

[24] V. M. Khmara, N. M. Kovtun, and G. A. Troitskii, Solid State Commun. **15**, 1769 (1974).

[25] M. Belakhovsky, M. Bogé, J. Chappert, and J. Sivardière, Solid State Commun. **20**, 473 (1976).

[26] G. C. Deng, P. Y. Guo, W. Ren, S. X. Cao, H. E. Maynard-Casely, M. Avdeev, and G. J. McIntyre, J. Appl. Phys. **117**, 164105 (2015).

[27] S. X. Cao, H. Z. Zhao, B. J. Kang, J. C. Zhang, and W. Ren, Sci. Rep. **4**, 5960 (2014).

[28] L. T. Tsymbal, Ya. B. Bazaliy, G. N. Kakazei, F. J. Palomares, and P. E. Wigen, IEEE Trans. Magn. **44**, 2933 (2008).

[29] T. Yamaguchi, J. Phys. Chem. Solids **35**, 479 (1974).

[30] D. Meier, H. Ryll, K. Kiefer, B. Klemke, J.-U. Hoffmann, R. Ramesh, and M. Fiebig, Phys. Rev. B **86**, 184415 (2012).

[31] A. I. Belyaeva and K. V. Baranova, J. Magn. Magn. Mater. **312**, 331 (2007).

[32] D. Treves, Phys. Rev. **125**, 1843 (1962).

[33] T. Susuki, N. Kurita, T. Tanaka, H. Nojiri, A. Matsuo, K. Kindo, and H. Tanaka, Phys. Rev. Lett. **110**, 267201 (2013).

[34] T. Ono, H. Tanaka, H. Aruga Katori, F. Ishikawa, H. Mitamura, and T. Goto, Phys. Rev. B **67**, 104431 (2003).

[35] G. Quirion, M. L. Plumer, O. A. Petrenko, G. Balakrishnan, and C. Proust, Phys. Rev. B **80**, 064420 (2009).

[36] Z. Jin, Z.-C. Xia, M. Wei, J.-H. Yang, B. Chen, S. Huang, C. Shang, H. Wu, X.-X. Zhang, J.-W. Huang, and Z.-W. Ouyang, J. Phys.: Condens. Matter **28**, 396002 (2016).

[37] M. F. Collins and O. A. Petrenko, Can. J. Phys. **75**, 605 (1997).

[38] H. Kawamura, Can. J. Phys. **79**, 1447 (2001).

[39] C. E. Johnson, L. A. Prelorendjo, and M. F. Thomas, J. Magn. Magn. Mater. **15–18**, 557 (1980).

[40] H. L. Wu, S. X. Cao, M. Liu, Y. M. Cao, B. J. Kang, J. C. Zhang, and W. Ren, Phys. Rev. B **90**, 144415 (2014).

[41] L. T. Tsymbal, G. N. Kakazei, and Ya. B. Bazaliy, Phys. Rev. B **79**, 092414 (2009).